

5. Penulis Anggota

by Pasyimi Pasyimi

Submission date: 07-Feb-2024 03:29PM (UTC+0700)

Submission ID: 2288628435

File name: 05-Artikel-2022-Penulis_Anggota.pdf (2.49M)

Word count: 6347

Character count: 32494



Three-dimensional flow modelling of air and particle in a low-density biomass combustor chamber at various declination angles of tangential and secondary air pipes

Soen Steven^a, Elvi Restiawaty^{a,b,c}, Pasymi Pasymi^d, Yazid Bindar^{a,b,e,*}

^a Department of Chemical Engineering, Faculty of Industrial Technology, Institut Teknologi Bandung, Bandung 40132, Indonesia

^b Department of Bioenergy Engineering and Chemurgy, Faculty of Industrial Technology, Institut Teknologi Bandung, Bandung 40132, Indonesia

^c Research Group on Design and Development of Chemical Engineering Processes, Faculty of Industrial Technology, Institut Teknologi Bandung, Bandung 40132, Indonesia

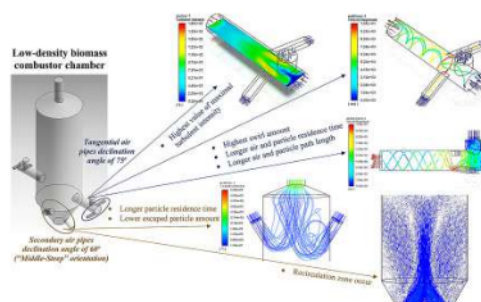
^d Department of Chemical Engineering, Faculty of Industrial Technology, Bung Hatta University, Padang, Indonesia

^e Research Group on Biomass and Food Processing Technology, Faculty of Industrial Technology, Institut Teknologi Bandung, Bandung 40132, Indonesia

HIGHLIGHTS

- The air-particle turbulent flow behavior is complex phenomena.
- CFD has been widely exploited to visualize the air-particle turbulent flow behavior.
- Tangential air pipe declination of 75° gives the most intense air-particle contact.
- Secondary air providence creates a recirculation zone in the combustor bottom area.
- Perfect air-particle contact is expected to complete biomass combustion conversion.

GRAPHICAL ABSTRACT



ARTICLE INFO

Keywords:
Biomass
Turbulence
Hydrodynamics
Recirculation
Residence time

ABSTRACT

Visual understanding of air and particle flow is important and useful in guiding biomass combustor design. This study investigates the effects of declination angles of tangential and secondary air pipes in a low-density biomass combustor chamber to achieve perfect contact between air and rice husk particle. The simulation was aided by computational fluid dynamics (CFD) method using the standard k-ε turbulent model. According to the result, tangential air pipes with a declination angle of 75° provide the most intense air-particle contact which is maximal turbulent intensity of 168%, swirl amount of 3.0–3.5, particle path length of 5.1 m, and particle residence time of 2.3 s. Furthermore, four secondary air pipes with a declination angle of 60° lower the escaped particle amount to 11.45% from previously 71.24%. This configuration can also create recirculation zones in the bottom area of the combustor which elevates the particle residence time to 766.9 s.

* Corresponding author at: Department of Chemical Engineering, Faculty of Industrial Technology, Institut Teknologi Bandung, Bandung 40132, Indonesia.
E-mail address: ybybyb@fti.itb.ac.id (Y. Bindar).

<https://doi.org/10.1016/j.powtec.2022.117883>

Received 2 July 2022; Received in revised form 18 August 2022; Accepted 22 August 2022

Available online 27 August 2022

0032-5910/© 2022 Published by Elsevier B.V.

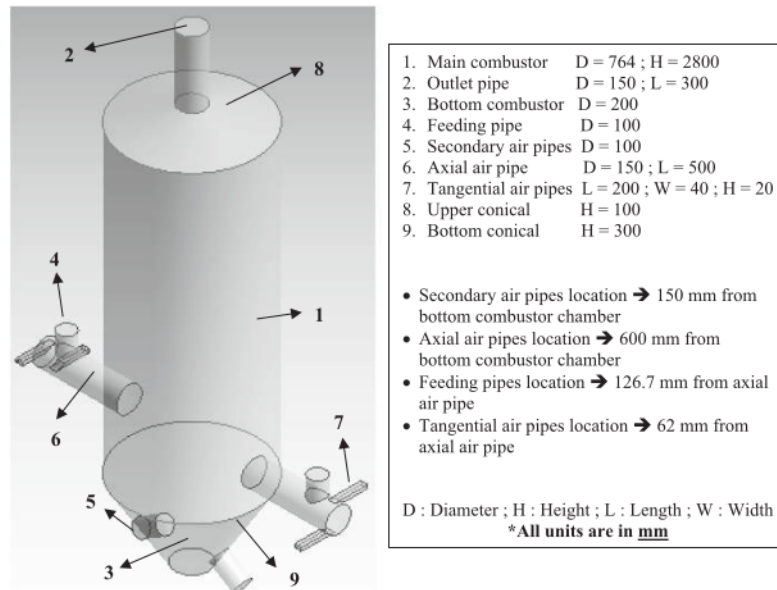


Fig. 1. The 3D sketch of low-density biomass combustor chamber.

1. Introduction

Currently, biomass utilization is widely applied for energy and chemical production purposes [1–7]. It is mostly carried out through biomass combustion [8–10], but poor mixing of air and particle in biomass combustor still occurs which leads to low combustion conversion [11,12]. This happens because of the not proper combustor geometry, inappropriate air supply technique, and incorrect burner dimension [9]. The aforementioned problems are induced by the complexity and uncomprehensive understanding of air-particle turbulent flow behavior [13–15]. In addition, insufficient experimental data and expensive instrumentation to validate it also affect [16,17].

At this time, fortunately, computational fluid dynamics (CFD) method has been widely exploited to reveal and visualize the complex air-particle turbulent flow behavior [17–19], predict the process performance [20–22], and validate the experimental result with the advantages of low cost and less time-consuming [23–26]. So far, there are several studies related to air and particle flow under the attendance of tangential and secondary air in the combustor chamber. The tangential air can generate swirl flow in the form of parabolic and helical patterns [27,28]. Meanwhile, the higher secondary airflow proportion improved the rice husk combustion efficiency in the fluidized bed combustor. It was reflected by a higher mean particle residence time in the combustor chamber of 52 s and lowering ash carbon content from 4.0% to 2.7% [9].

Subsequently, Koksai (2001) confirmed that providing secondary air in the circulating fluidized bed boiler alters the circulation rate, degree of mixing, and particle distribution [29]. Nemoda et al. (2005) also found the high recirculation effect and swirl intensity of flow structure in the swirl combustor under the providence of tangential air [24]. On the other hand, Ziqiang et al. (2016) claimed that a swirl combustor with four tangential inlet pipes with a slope of 30° produces the highest swirl intensity of air and particle [30]. Other than that, Pasymi et al. (2018) investigated that turbulence intensity is influenced by the rectangular two-tangential inlet orientation and the angle of 20° potentially results in the best performance [31].

From the above exposition, there are still few studies that focused on the effects of declination angles of tangential and secondary air pipes on the performance of a low-density biomass combustor [14,23,32]. This

present study, hence, is aimed to observe the turbulent intensity profile, air and particle flow pattern, swirl amount, particle path length, particle residence time, and recirculation zones existence under various tangential and secondary air pipes declination angles, complete with their flow visualization. The employed biomass was rice husk. Model validation, mesh sensitivity analysis, and grid independence test were conducted before the main simulation was implemented. Afterward, the visualization of air and particle flow in the combustor chamber was also served. The orientation that gives the greatest turbulence was finally chosen and discussed.

2. Methodology

2.1. Geometry and simulation condition

The combustor chamber has a main diameter of 764 mm and a total height of 2800 mm. The diameter for outlet pipe, bottom biomass combustor, feeding pipes, and secondary air pipes are 150 mm, 200 mm, 100 mm, and 100 mm, successively. The secondary air pipes are located at 150 mm from the bottom of the combustor. The outlet pipe has a length of 300 mm whereas the combustor has upper and lower conical zones with the height of 100 mm and 300 mm, in respective terms. The burner diameter is 150 mm and has 500 mm in length with the position measured at 600 mm from the bottom of the combustor. The feeding pipes as well as the tangential air pipes (200 mm in length, 40 mm in width, and 20 mm in height) are located at 126.7 mm and 62 mm from the axial air supply. The detailed sketch and dimension for combustor geometry are served in Fig. 1.

The simulation was performed in absence of combustion phenomena or usually named cold flow simulation [26,33]. As a consequence, the operating temperature is 25 °C. Rice husk, as the utilized low-density biomass particle in this study, was injected at 1 t/h of loading rate. It has particle density of 662 kg/m³, sphericity of 0.5, and homogeneous size distribution with a mean diameter of 2.5 mm. Also, the interaction of air and particle was presumed not to generate rotational flow. In further, this study used 80% of excess air and the ultimate analysis of rice husk was 46.92% C, 6.69% H, 45.20% O, and 1.19% N. Based on calculations carried out by Steven et al. (2022), the mass ratio of air and

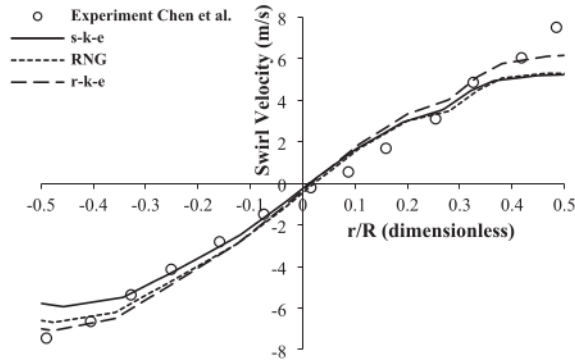


Fig. 2. Swirl velocity profile under k - ϵ turbulent models vs. experiment by Chen et al. (1999).

biomass under this condition is 10 [34]. The air supply was distributed in axial, feeding, secondary, and tangential air with the proportion of 20%, 5%, 30%, and 45%, respectively. Furthermore, the air flowrate for upper secondary air (U_{su}) is varied equal to and larger than the lower secondary air (U_{sl}) with a factor of 2.57. The turbulent intensity and

turbulent viscosity ratio at every boundary condition were set at 10%.

2.2. Mathematical model

The time-averaged of fluid flow is calculated using the standard k - ϵ turbulent model, a derivative group of Reynolds-Averaged Navier-Stokes [25,35,36]. The equation for mass conservation is written in eq. 1 and momentum conservation in three-dimensional directions as in eq. 2. The momentum conservation contains turbulent viscosity term which is described in the forms of k and ϵ [37,38], as written in eq. 3. The k variable itself is served in eq. 4 whereas eq. 5 is for determining ϵ variable. Another turbulence variable, turbulent intensity, is stated in eq. 6 [39]. A standard wall function is also employed to evaluate the

Table 1

Performance comparisons of tetrahedral and hexagonal mesh.

Element Size	Geometry	Nodes	Elements	Mesh Generation Time (s)	
				Trial 1	Trial 2
1 mm	Tetrahedral	126,853	87,538	9.7	9.3
	Hexagonal	87,090	25,731	46.3	45.4
1.5 mm	Tetrahedral	39,455	26,217	6.7	6.4
	Hexagonal	29,204	8856	38.1	38.3

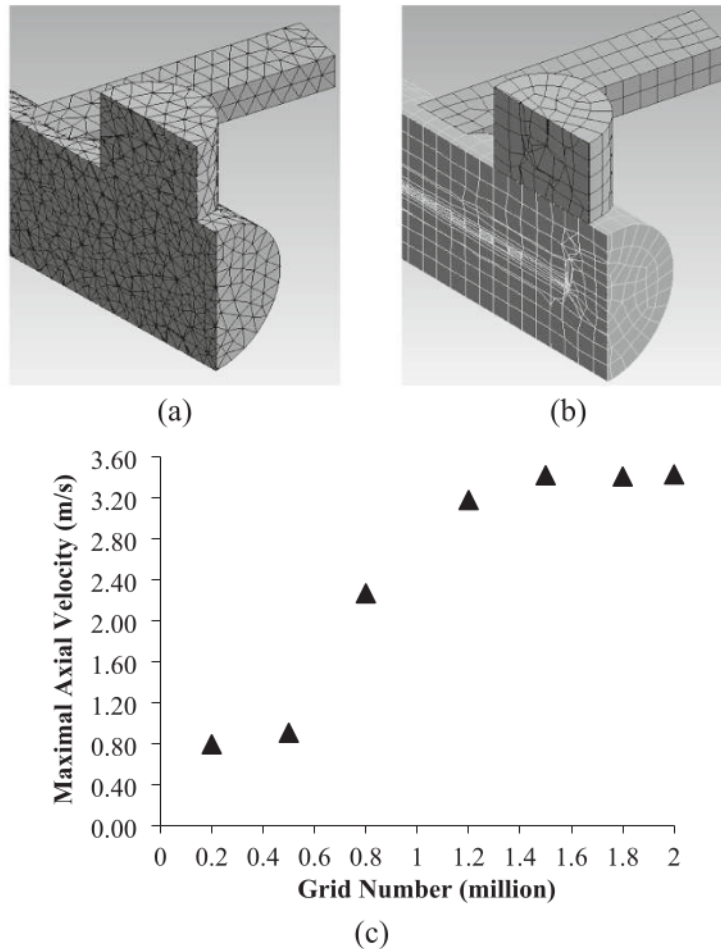


Fig. 3. Tetrahedral (a) and hexagonal (b) mesh geometries in the burner part; Grid independence test for this study (c).

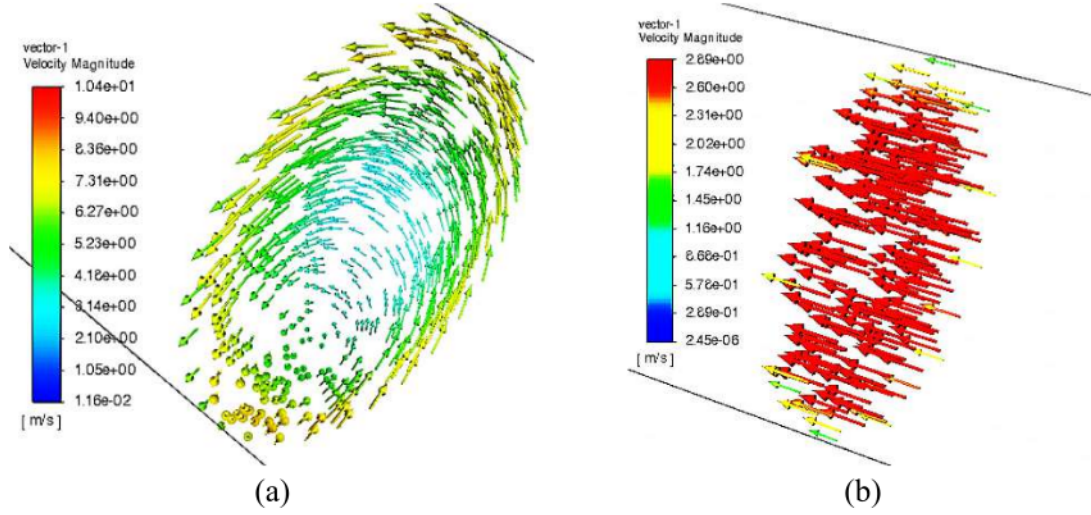


Fig. 4. Air velocity vector in the burner with tangential air (a) and without tangential air (b).

condition near the wall.

$$\frac{\partial \rho}{\partial t} + \frac{\partial (\rho \bar{u}_x)}{\partial x} + \frac{\partial (\rho \bar{u}_y)}{\partial y} + \frac{\partial (\rho \bar{u}_z)}{\partial z} = 0 \quad (1)$$

$$\rho \frac{\partial \bar{u}_x}{\partial t} + \rho \bar{u}_x \frac{\partial \bar{u}_x}{\partial x} + \rho \bar{u}_y \frac{\partial \bar{u}_x}{\partial y} + \rho \bar{u}_z \frac{\partial \bar{u}_x}{\partial z} = -\frac{\partial \bar{p}}{\partial x} + \frac{\partial}{\partial x} \left[(\mu + \mu_t) \frac{\partial \bar{u}_x}{\partial x} \right] + \frac{\partial}{\partial y} \left[(\mu + \mu_t) \frac{\partial \bar{u}_x}{\partial y} \right] + \frac{\partial}{\partial z} \left[(\mu + \mu_t) \frac{\partial \bar{u}_x}{\partial z} \right] + \rho g_x + F_{ex} \quad (2a)$$

$$\rho \frac{\partial \bar{u}_y}{\partial t} + \rho \bar{u}_x \frac{\partial \bar{u}_y}{\partial x} + \rho \bar{u}_y \frac{\partial \bar{u}_y}{\partial y} + \rho \bar{u}_z \frac{\partial \bar{u}_y}{\partial z} = -\frac{\partial \bar{p}}{\partial y} + \frac{\partial}{\partial x} \left[(\mu + \mu_t) \frac{\partial \bar{u}_y}{\partial x} \right] + \frac{\partial}{\partial y} \left[(\mu + \mu_t) \frac{\partial \bar{u}_y}{\partial y} \right] + \frac{\partial}{\partial z} \left[(\mu + \mu_t) \frac{\partial \bar{u}_y}{\partial z} \right] + \rho g_y + F_{ey} \quad (2b)$$

$$\rho \frac{\partial \bar{u}_z}{\partial t} + \rho \bar{u}_x \frac{\partial \bar{u}_z}{\partial x} + \rho \bar{u}_y \frac{\partial \bar{u}_z}{\partial y} + \rho \bar{u}_z \frac{\partial \bar{u}_z}{\partial z} = -\frac{\partial \bar{p}}{\partial z} + \frac{\partial}{\partial x} \left[(\mu + \mu_t) \frac{\partial \bar{u}_z}{\partial x} \right] + \frac{\partial}{\partial y} \left[(\mu + \mu_t) \frac{\partial \bar{u}_z}{\partial y} \right] + \frac{\partial}{\partial z} \left[(\mu + \mu_t) \frac{\partial \bar{u}_z}{\partial z} \right] + \rho g_z + F_{ez} \quad (2c)$$

$$\mu_t = C_\mu \rho \frac{k^2}{\varepsilon} \quad (3)$$

$$\rho \frac{\partial k}{\partial t} + \rho \bar{u}_x \frac{\partial k}{\partial x} + \rho \bar{u}_y \frac{\partial k}{\partial y} + \rho \bar{u}_z \frac{\partial k}{\partial z} = \frac{\partial}{\partial x} \left[\left(\mu + \frac{\mu_t}{\sigma_k} \right) \frac{\partial k}{\partial x} \right] + \frac{\partial}{\partial y} \left[\left(\mu + \frac{\mu_t}{\sigma_k} \right) \frac{\partial k}{\partial y} \right] + \frac{\partial}{\partial z} \left[\left(\mu + \frac{\mu_t}{\sigma_k} \right) \frac{\partial k}{\partial z} \right] + G_k - Y_k \quad (4a)$$

$$G_k = 2\mu_t \left[\left(\frac{\partial \bar{u}_x}{\partial x} \right)^2 + \left(\frac{\partial \bar{u}_y}{\partial y} \right)^2 + \left(\frac{\partial \bar{u}_z}{\partial z} \right)^2 \right] + \mu_t \left(\frac{\partial \bar{u}_x}{\partial y} + \frac{\partial \bar{u}_y}{\partial x} \right)^2 + \mu_t \left(\frac{\partial \bar{u}_x}{\partial z} + \frac{\partial \bar{u}_z}{\partial x} \right)^2 + \mu_t \left(\frac{\partial \bar{u}_y}{\partial z} + \frac{\partial \bar{u}_z}{\partial y} \right)^2 \quad (4b)$$

$$Y_k = \rho \varepsilon \quad (4c)$$

$$\rho \frac{\partial \varepsilon}{\partial t} + \rho \bar{u}_x \frac{\partial \varepsilon}{\partial x} + \rho \bar{u}_y \frac{\partial \varepsilon}{\partial y} + \rho \bar{u}_z \frac{\partial \varepsilon}{\partial z} = \left[\left(\mu + \frac{\mu_t}{\sigma_\varepsilon} \right) \frac{\partial \varepsilon}{\partial x} \right] + \frac{\partial}{\partial y} \left[\left(\mu + \frac{\mu_t}{\sigma_\varepsilon} \right) \frac{\partial \varepsilon}{\partial y} \right] + \frac{\partial}{\partial z} \left[\left(\mu + \frac{\mu_t}{\sigma_\varepsilon} \right) \frac{\partial \varepsilon}{\partial z} \right] + C_{\varepsilon 1} \frac{\varepsilon}{k} G_k - C_{\varepsilon 2} \rho \frac{\varepsilon^2}{k} \quad (5)$$

$$I_T = \frac{u'_{RMS}}{\bar{u}} = \frac{\sqrt{\frac{(u'_x)^2 + (u'_y)^2 + (u'_z)^2}{3}}}{\sqrt{\frac{(\bar{u}_x)^2 + (\bar{u}_y)^2 + (\bar{u}_z)^2}{3}}} \quad (6)$$

where p is static pressure, ρ is fluid density, μ is fluid viscosity, g is gravitational acceleration constant, F_e is external force, μ_t is turbulent viscosity, k is turbulent kinetic energy, ε is turbulent kinetic dissipation rate, I_T is turbulent intensity, u'_{RMS} is root mean square of velocity fluctuation, \bar{u} is average velocity, and constants value for $C_\mu = 0.09$, $\sigma_k = 1.0$, $\sigma_\varepsilon = 1.3$, $c_{\varepsilon 1} = 1.44$, and $c_{\varepsilon 2} = 1.92$.

On the other side, the particle flow in a fluid flow field was defined in the discrete phase model which has continuous phase and particle phase. The continuous phase is modeled by Eulerian method while the particle phase is modeled by the Lagrangian method [37]. For every particle which has a density ρ_p , diameter d_p and sphericity factor φ_p , the particle velocity field has components of \bar{u}_{px} , \bar{u}_{py} , and \bar{u}_{pz} . The particle velocities are influenced only by particle-fluid drag force which is formulated by a drag equation. The equation for drag coefficient (C_D) is shown in eq. 7 [40] and the particle momentum conservation in i^{th} direction ($i = x, y, z$) is presented in eq. 8 [26,41].

$$C_D = \frac{\beta_1 Re_{p,i}}{\beta_2 + Re_{p,i}} + \frac{24}{Re_{p,i}} (1 + \beta_3 Re_{p,i}^{\beta_4}) \quad (7a)$$

$$Re_{p,i} = \frac{\rho d_p (\bar{u}_i - \bar{u}_p)}{\mu} \quad (7b)$$

$$\beta_1 = \exp(4.905 - 13.894 \varphi_p + 18.422 \varphi_p^2 - 10.260 \varphi_p^3)$$

$$\beta_2 = \exp(1.468 + 12.258 \varphi_p - 20.732 \varphi_p^2 + 15.885 \varphi_p^3)$$

$$\beta_3 = \exp(2.329 - 6.458 \varphi_p + 2.449 \varphi_p^2)$$

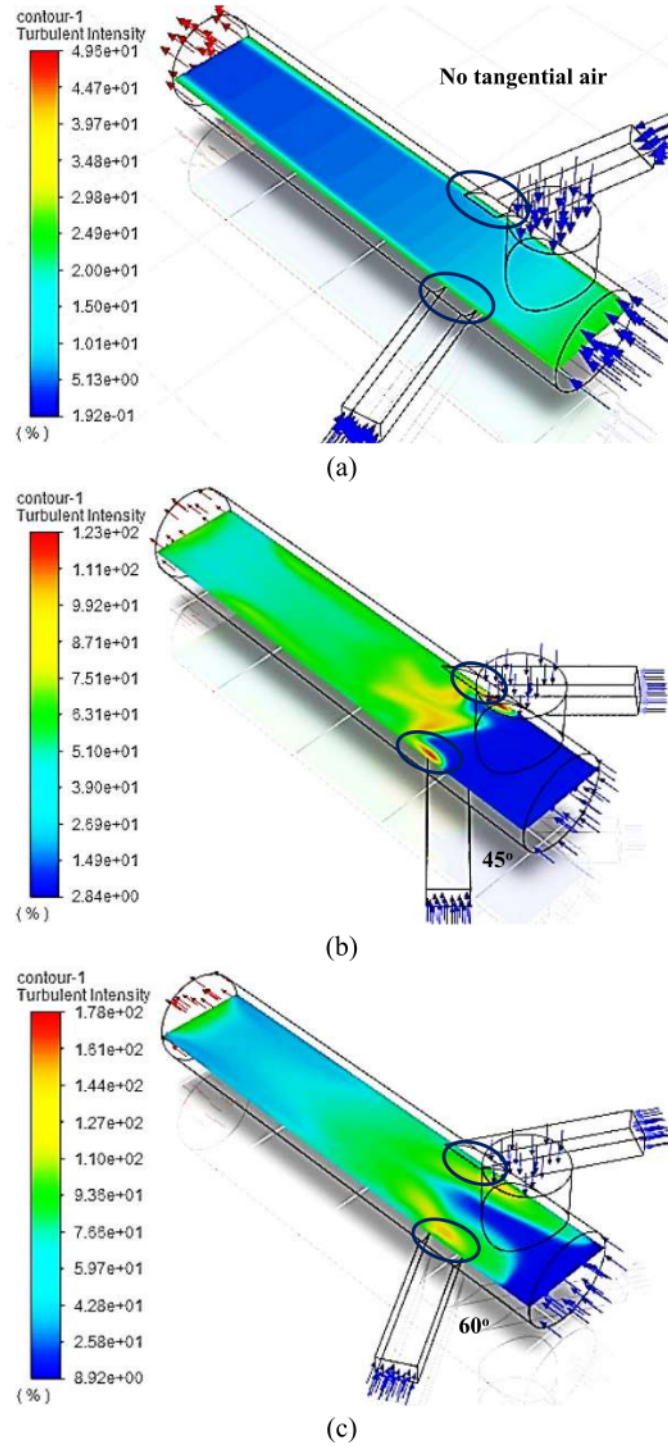


Fig. 5. Turbulent intensity in the burner under no tangential air (a); with tangential air under tangential air pipes declination angle of 45° (b), 60° (c), and 75° (d).

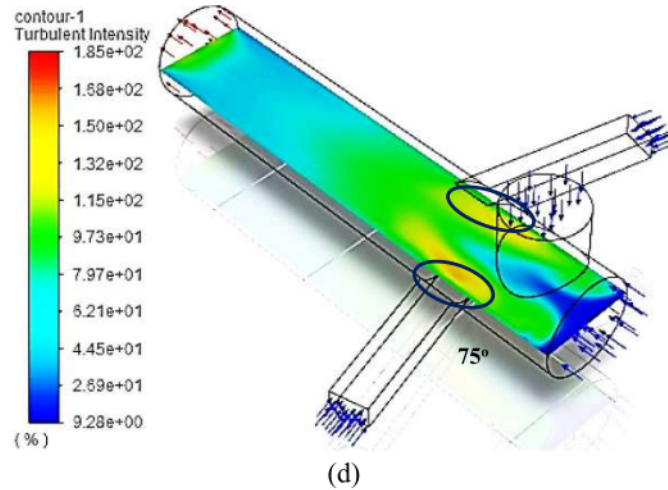


Fig. 5. (continued).

$$\beta_4 = 0.096 + 0.556\phi_p \quad (7c)$$

$$\frac{\partial \bar{u}_{pi}}{\partial t} = (\bar{u}_i - \bar{u}_{pi}) \left(\frac{3\mu C_p Re_{pi}}{4\rho_p d_p^2} \right) + \frac{\rho_p - \rho}{\rho_p} g_i + F_{ei} \quad (8)$$

2.3. Numerical solution setup

The problem was computed using ANSYS Fluent 2021. The pressure-based steady-state solving method used a coupled algorithm for pressure-velocity coupling. The spatial discretization methods consist of least square cell-based for gradient, second-order upwind for momentum, second-order for pressure, and first-order upwind for both k and ϵ . The relaxation factor was taken from ANSYS default values which were 0.5 for pressure, 0.5 for momentum, 1 for density, 1 for body forces, 0.75 for turbulent kinetic energy, 0.75 for turbulent dissipation rate, and 1 for turbulent viscosity. The convergence criteria were set at 10^{-6} to guarantee minimal error. The pseudo-transient calculation was performed for 1000 iterations under the automatic time-step method and time scale factor 1.

3. Results and discussion

3.1. Model initial validation, mesh sensitivity analysis, and grid independence test

The standard $k-\epsilon$ turbulent model was validated by swirl flow experiment in a 10,000 mm horizontal pipe by Chen et al. (1999) [42]. This experiment is chosen due to its simple geometry, dimension clarity, and complete information. The pipe diameter was 146 mm and was equipped with two tangential pipes which were located at 1000 mm after the axial inlet. The length of tangential pipe was 3000 mm. Air axial inlet was conditioned to produce a Reynold number (Re) of 100,000. The axial and tangential air ratio was 0.8 and the swirl velocity was measured in the location at 1930 mm after the air axial inlet. The grid number used was 1,480,000.

Besides, validation using RNG and realizable $k-\epsilon$ turbulent models were also performed under a similar grid number. The simulation result under three turbulent models is compared to the experimental data, as shown in Fig. 2. This figure interprets that all $k-\epsilon$ turbulent models provide precision results and are somewhat close to the experiment. Basically, the accuracy of $k-\epsilon$ turbulent models become low when

predicting the flow near the wall [37,43], but this study does not intend to scrutinize the phenomenon near the wall. Since the good performance in predicting the swirl and fully turbulent conditions and less demanding computation cost [44], the standard $k-\epsilon$ turbulent model becomes quite superior to other models and is no doubt to be selected in this study. In addition, this turbulent model is also broadly utilized for fluid flow modelling in industrial and engineering aspects [26,45].

After the performance of standard $k-\epsilon$ turbulent model is validated, the mesh sensitivity analysis for this study is then implemented to evaluate the lowest-intensive computation. The mesh geometry is generated in the form of tetrahedral and hexagonal. Each of them has an element size that is varied at 1 mm and 1.5 mm. The result shows that hexagonal mesh generation requires about 5.5 fold longer than tetrahedral. Under equal element size, the amount of nodes and elements in the hexagonal mesh is lesser than tetrahedral. In another word, tetrahedral mesh gives more accurate calculation as well as less computation time compared to hexagonal [46]. The mesh result in the burner part is given in Fig. 3a-b and the performance comparison is tabulated in Table 1.

The grid independence test of the combustor chamber is finally employed using standard $k-\epsilon$ turbulent model and mesh geometry of tetrahedral. The grid number varied at 200,000, 500,000, 800,000, 1,200,000, 1,500,000, 1,800,000, and 2,000,000. The identified variable was the maximal axial velocity at the radial position of combustor chamber for a height of 2000 mm from the bottom. Based on Fig. 3c, the value of maximal axial velocity still significantly changes under coarse grid numbers (200,000, 500,000, 800,000, and 1,200,000). The maximal axial velocity is obtained at 3.42 m/s at a grid number of 1,500,000 and finer grid numbers (1,800,000 and 2,000,000) have given a meaningless discrepancy. Therefore, the optimal grid number chosen and used for this simulation is 1,500,000.

3.2. Effects of tangential air pipes declination angles

It is revealed that providing tangential air could generate swirl flow in the burner, as expressed in Fig. 4a. The tangential air flow through the burner wall is reflected in a circular velocity vector [47]. The velocity has a maximal value of 6.27 m/s at the wall and is reduced to 3.14 m/s at the center. In absence of tangential air supply, the air velocity profile changes to a pattern similar to the turbulent regime flow profile, as depicted in Fig. 4b. The vector is indicated only in axial directions. For only axial air supply, the maximal velocity values are 2.89 m/s at the

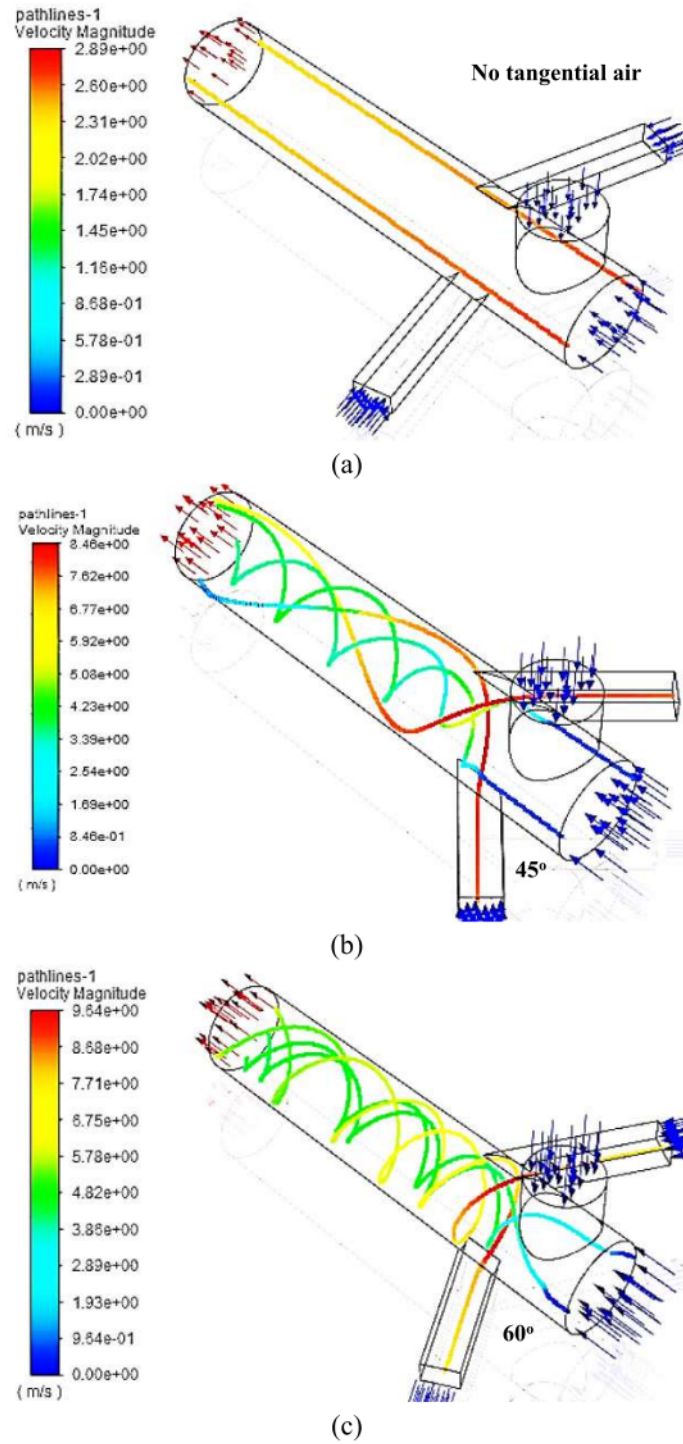


Fig. 6. Air pathline profile under no tangential air (a); with tangential air under tangential air pipes declination angle of 45° (b), 60° (c), and 75° (d).

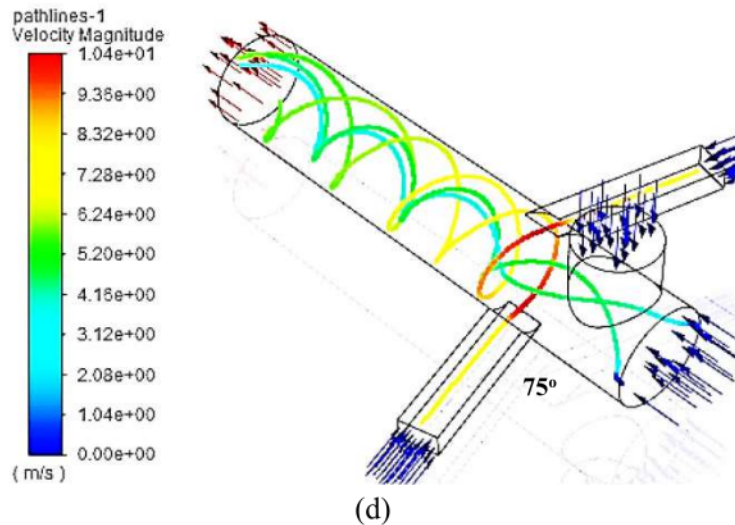


Fig. 6. (continued).

center and reduced to 1.45 m/s at the wall.

The appropriate tangential air supply is aimed to create high turbulence and generate perfect contact between air and particle. It is strongly affected by declination angle which is varied at 45°, 60°, and 75°. The turbulence variables in the burner encompass turbulent intensity, swirl amount, particle residence time, and particle path length. The simulation was held for all declination angles and also under no tangential air condition as a comparison. Based on the result, the maximal values of turbulent intensity lie on the intersection area of the tangential inlet, as shown in the blue signs in Fig. 5. In absence of tangential air supply, the maximal turbulent intensity has the lowest value, 25%. The highest value is 168% for tangential air pipes of 75°, then followed by tangential air pipes of 60° with the value of 162% and tangential air pipes of 45° with the value of 123%. It turns out that the broader declination angle of tangential air pipes intensifies the incidence of flow collision.

In addition, the visualization in the form of air pathline profiles indicates that the flow is concentrated in axial direction when only axial air is provided. On the other hand, the profiles transform to have a swirling pattern under the presence of tangential air [28,48]. The swirl is graphically determined by the number of waves formed [27]. The more intense the turbulence, the higher amount of swirl is obtained, as reflected in Fig. 6. The declination angles of 45°, 60°, and 75° generate the air swirl amount of 1.5–2.5, 2.5–3.0, and 3.0–3.5, sequentially.

Subsequently, the visualization in the form of particle flow patterns is strongly affected by air flow profile. In absence of tangential air, consequently, particle flow is only found along the axial direction of the burner. In line with Fig. 7a, there is a weak wavy flow pattern that is not categorized as a swirl. It is caused by particle and wall reflection [37]. The particle flow direction in the burner becomes more complex when tangential air is provided. It can be further decomposed in axial, tangential, and radial directions [33]. In visual, particle swirl amount for tangential air pipes with declination angles of 45°, 60°, and 75° is 1.5–2.0, 2.5–3.0, and 3.0–3.5, as visualized in Fig. 7b–d.

For declination angles of 45°, the net air velocity direction is more dominant in axial direction in lieu of tangential and radial directions. The net air velocity is distributed in axial, tangential, and radial directions when the declination angle is increased to 75°, which consequently produces more swirl amount. This condition leads to a longer biomass path length and has an impact on greater biomass residence time in the burner indeed, and vice versa [41,49]. This figure also

implies the particle flow pattern is strongly affected by the particle fall position and causes the appearance of multiple particle trajectories.

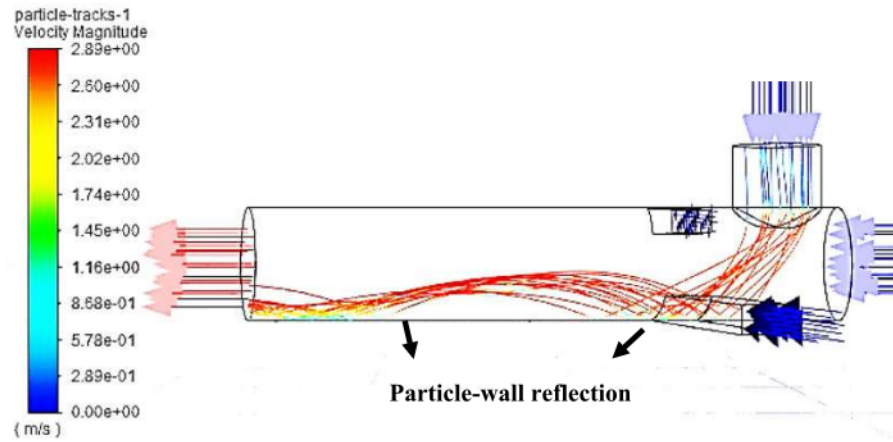
The existence of tangential air elongates the particle path length from 0.81 m to 5.10 m. This resulted in a longer particle residence time from 0.3 s to 2.3 s. For combustion purposes, enhancing particle residence time can increase the combustion conversion [50,51]. Thus, the tangential air pipes with a declination angle of 75° provide the highest turbulent intensity, highest swirl amount, longest path length, and greatest residence time for both air and particle flow, as summarized in Table 2. It shows that for all variations, the average particle velocity is nearly similar. The higher turbulent intensity, at a constant value of average velocity, implies higher velocity fluctuation. Higher velocity fluctuation is in line with the more swirl amount recorded.

3.3. Effects of secondary air pipe declination angles

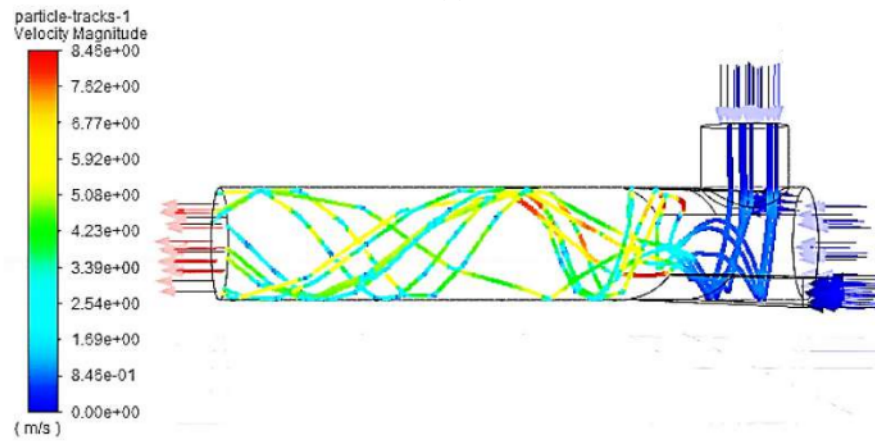
The secondary air pipes are located at the bottom area of the combustor chamber. They have an initial declination angle of 32°, namely gradual type. At first, the simulation result reveals that the escaped particle is 71.24%. To overcome this problem, the combustor is then modified by adding two upper secondary pipes with varying orientations: top-gradual, top-steep, middle-gradual, and middle-steep. The steep type is the secondary air pipes with a declination angle of 60°. Upper secondary air pipes for the top type are located at 2350 mm from the bottom whilst the middle type is at 2000 mm from the bottom. The attendance of upper secondary air pipes is believed can recirculate the particle back into the combustor chamber and thereby giving a longer particle residence time [9,27,52].

Installing upper secondary air in the combustor is proven to create particle recirculation which is reflected in the reduction of escaped particle amounts far below 71.24%. Providing the secondary air pipes with upper flowrate of 2.57 times greater than lower one can also dampen the escaped particle from 27.25% to 22.30% for top-gradual; 16.10% to 15.88% for top-steep; 56.36% to 36.88% for middle-gradual; and 13.74% to 11.45% for middle-steep. The steeper declination angle exhibits a lower escaped particle and gives a higher particle residence time in the combustor chamber, as plotted in Fig. 8.

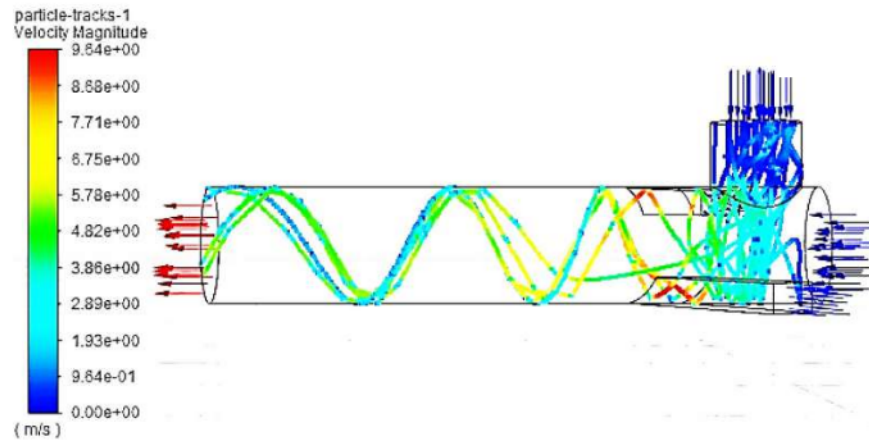
The steeper declination angle of secondary air pipes maximizes the particle recirculation back into the combustor chamber while the gradual type offers a weaker recirculation, as seen in the red sign in Fig. 9a–d. Additionally, the top orientation of upper secondary air pipes is not able to push back the particle into the combustor chamber.



(a)



(b)



(c)

Fig. 7. Particle flow pattern under no tangential air (a); with tangential air under tangential air pipes declination angle of 45° (b), 60° (c), and 75° (d).

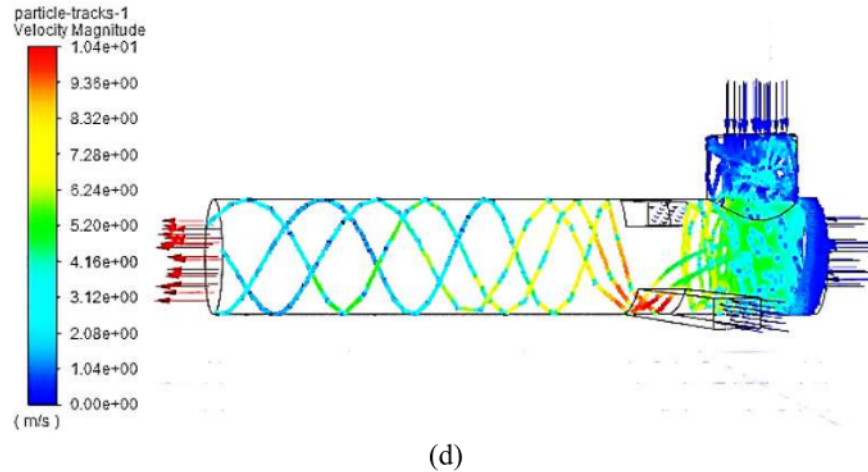


Fig. 7. (continued).

Table 2
Effects of tangential air pipes declination angle on burner performance parameters.

Parameter	Tangential Air Providing			
	No	Yes	Yes	Yes
Tangential air pipes declination (°)	–	45	60	75
Maximal turbulent intensity (%)	25	123	161	168
Swirl amount	0	1.5–2.5	2.5–3.0	3.0–3.5
Particle path length (m)	0.81	1.35	2.36	5.10
Particle residence time (s)	0.3	0.6	1.0	2.3
Average particle velocity (m/s)	2.38	2.25	2.40	2.25

According to the previous figure, the lowest escaped particle (11.45%), as well as the highest particle residence time (766.9 s), is nominated to the secondary pipes with middle-steep orientation, strengthening the

qualitative explanation. This condition supports the middle-steep as the most suitable secondary air pipe orientation.

Apart from that, the presence of secondary air generates the recirculation zone in the bottom area of the combustor chamber [9,41]. It enhances the particle residence time and is expected to increase the biomass combustion conversion [52]. The recirculation zone due to secondary air is presented in Fig. 9e. Meanwhile, there is a nil recirculation zone under no secondary air supply, as seen in Fig. 9f. It lessens the air and particle contact so as to increase the possibility of uncombusted particles in the combustor chamber [9,41]. For the middle-steep type, the recirculation zone in the combustor bottom area augments the particle residence time to 766.9 s from the initial 564.0 s under no secondary air. The same pattern with a different value when compared to Rozainee et al. (2010), recorded at 52 s [9]. It happens because the larger combustor dimension in this study creates a longer particle residence time.

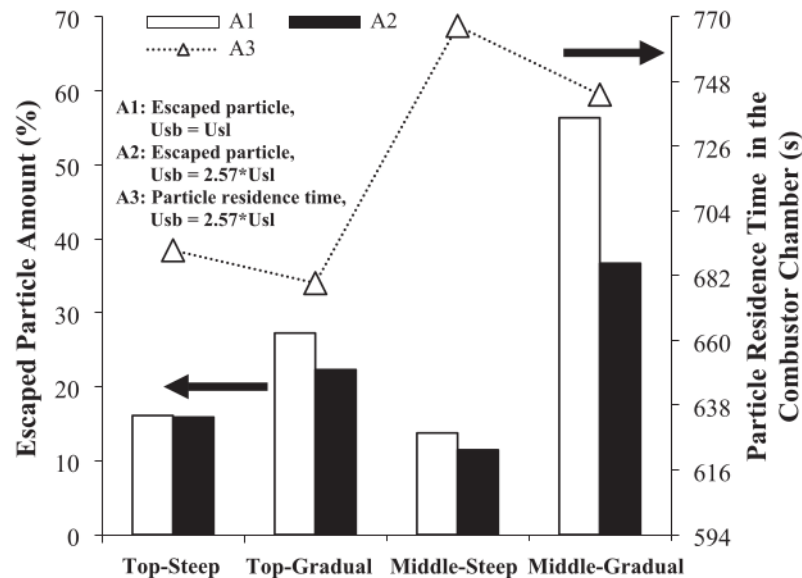


Fig. 8. The performance comparisons of biomass combustor under various orientations of secondary air pipes.

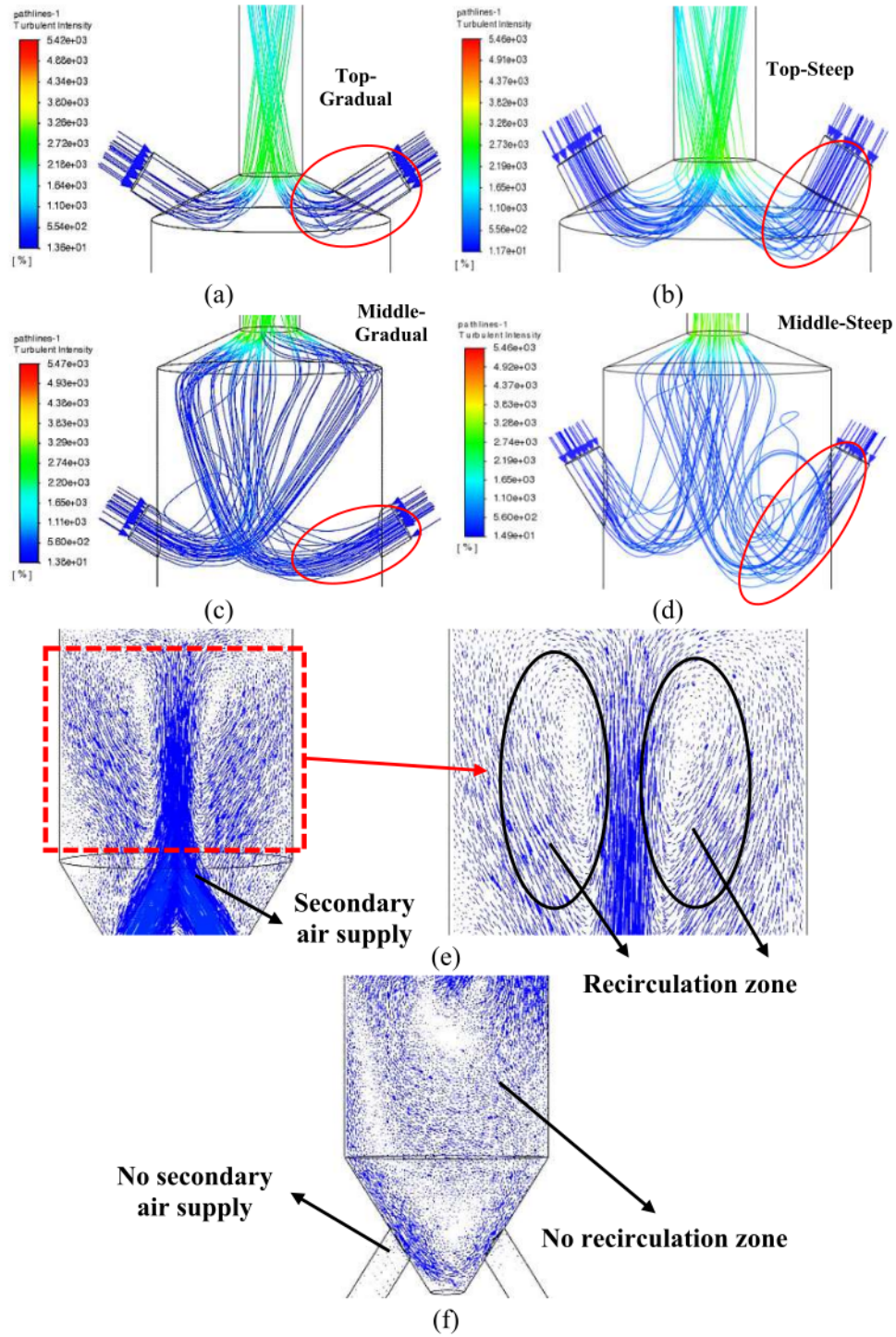


Fig. 9. Turbulent intensity under various secondary air pipes orientations (a-d); Recirculation zone in the bottom area of combustor chamber with (e) and without (f) secondary air.

4. Conclusions

The flow behavior of air and rice husk particle in low-density biomass combustor under various declination angles of tangential and secondary air pipes have been visualized and analyzed through the CFD method. Providing tangential air pipes with a declination angle of 75° increases the particle path length from 0.81 m to 5.10 m, elongates the particle residence time from 0.3 s to 2.3 s, enhances the turbulent intensity from 25% to 168%, and produces swirl amount of 3.0–3.5. Moreover, the addition of upper secondary air pipes with a “middle-steep” orientation reduces the escaped particle amount from 71.24% to 11.45%. The presence of secondary air also increases the air-particle contact as a result of the creation of a recirculation zone at the bottom area of the combustor. This is evident from the longer particle residence time from 564.0 s to 766.9 s. Under the meant configuration of combustor chamber, air and rice husk particle contact becomes intense and is expected to rectify biomass combustion conversion. Conclusively, this study verifies that the CFD method can be a guide for designing high-performance industrial biomass combustor.

CRediT authorship contribution statement

Soen Steven: Visualization, Data curation, Investigation, Methodology, Writing - original draft, Writing - review & editing. **Elvi Restiawaty:** Formal analysis, Supervision. **Yazid Bindar:** Conceptualization, Supervision, Funding acquisition. **Pasymi Pasymi:** Formal analysis.

Declaration of Competing Interest

The authors report there are no competing interests to declare.

Data availability

No data was used for the research described in the article.

Acknowledgments

We would like to greatly acknowledge the Riset Unggulan PT grants funding, Indonesian Ministry of Research and Technology/National Research and Innovation Agency for the full financial support to this study. Many thanks to Mr. Imam Mardhatillah Fajri for the assistance in operating ANSYS Fluent. Not to forget, the authors also appreciate Mr. Harben (Biomass Technology Workshop ITB Jatininggor) for his kindness and help in conceptualizing the biomass combustor design.

References

- [1] P. Hernowo, S. Steven, E. Restiawaty, A. Irawan, C.B. Rasrendra, S. Marno, Y. Meliana, Y. Bindar, Chemicals component yield prediction and kinetic parameters determination of oil palm shell pyrolysis through volatile state approach and experimental study, *J. Anal. Appl. Pyrolysis* 161 (2022), 105399, <https://doi.org/10.1016/j.jaap.2021.105399>.
- [2] Y. Ramli, S. Steven, E. Restiawaty, Y. Bindar, Simulation study of bamboo leaves valorization to small-scale electricity and bio-silica using ASPEN PLUS, *Bioenerg. Res.* (2022) 1–9, <https://doi.org/10.1007/s12155-022-10403-7>.
- [3] P. Hernowo, C.B. Rasrendra, A. Irawan, S. Marno, Y. Meliana, O. Muraza, Y. Bindar, Volatile state mathematical models for predicting components in biomass pyrolysis products, *J. Eng. Technol. Sci.* 54 (2022), 220108, <https://doi.org/10.5614/j.eng.technol.sci.2022.54.1.8>.
- [4] Y. Bindar, S. Steven, S.W. Kresno, P. Hernowo, E. Restiawaty, R. Purwadi, T. Prakoso, Large-scale pyrolysis of oil palm frond using two-box chamber pyrolyzer for cleaner biochar production, *Biomass Conv. Bioref.* (2022), <https://doi.org/10.1007/s13399-022-02842-1>.
- [5] S. Steven, E. Restiawaty, Y. Bindar, Operating variables on production of high purity bio-silica from rice hull ash by extraction process, *J. Eng. Technol. Sci.* 54 (2022), 220304, <https://doi.org/10.5614/j.eng.technol.sci.2022.54.3.4>.
- [6] Y.W. Budhi, M. Effendy, Y. Bindar, S. Subagio, Dynamic behavior of reverse flow reactor for lean methane combustion, *J. Eng. Technol. Sci.* 46 (2014) 299–317, <https://doi.org/10.5614/j.eng.technol.sci.2014.46.3.5>.
- [7] S. Steven, E. Restiawaty, P. Pasymi, Y. Bindar, Influences of pretreatment, extraction variables, and post treatment on bench-scale rice husk black ash (RHBA) processing to bio-silica, *Asia-Pac. J. Chem. Eng.* 16 (2021), e2694, <https://doi.org/10.1002/apj.2694>.
- [8] P. Ostermeier, F. Fischer, S. Fendt, S. DeYoung, H. Spliethoff, Coarse-grained CFD-DEM simulation of biomass gasification in a fluidized bed reactor, *Fuel* 255 (2019), 115790, <https://doi.org/10.1016/j.fuel.2019.115790>.
- [9] M. Rozainee, S.P. Ngo, A.A. Salema, K.G. Tan, Computational fluid dynamics modeling of rice husk combustion in a fluidized bed combustor, *Powder Technol.* 203 (2010) 331–347, <https://doi.org/10.1016/j.powtec.2010.05.026>.
- [10] H.C. Park, H.S. Choi, Numerical study of the segregation of pyrolyzed char in a bubbling fluidized bed according to distributor configuration, *Powder Technol.* 355 (2019) 637–648, <https://doi.org/10.1016/j.powtec.2019.07.084>.
- [11] J. Werther, M. Saenger, E.U. Hartge, T. Ogada, Z. Siagi, Combustion of agricultural residues, *Prog. Energy Combust. Sci.* 26 (2000) 1–27, [https://doi.org/10.1016/S0360-1285\(99\)00005-2](https://doi.org/10.1016/S0360-1285(99)00005-2).
- [12] S. Steven, E. Restiawaty, Y. Bindar, Simple mass transfer simulation using a single-particle heterogeneous reaction approach in rice husk combustion and rice husk ash extraction, *IOP Conf. Ser. Earth Environ. Sci.* 963 (2022), 012050, <https://doi.org/10.1088/1755-1315/963/1/012050>.
- [13] A.A. Bhuiyan, J. Naser, CFD modelling of co-firing of biomass with coal under oxy-fuel combustion in a large scale power plant, *Fuel* 159 (2015) 150–168, <https://doi.org/10.1016/j.fuel.2015.06.058>.
- [14] Y. Guan, J. Chang, K. Zhang, B. Wang, Q. Sun, Three-dimensional CFD simulation of hydrodynamics in an interconnected fluidized bed for chemical looping combustion, *Powder Technol.* 268 (2014) 316–328, <https://doi.org/10.1016/j.powtec.2014.08.046>.
- [15] S. Yang, K. Luo, K. Zhang, K. Qiu, J. Fan, Numerical study of a lab-scale double slot-rectangular spouted bed with the parallel CFD-DEM coupling approach, *Powder Technol.* 272 (2015) 85–99, <https://doi.org/10.1016/j.powtec.2014.11.035>.
- [16] E.E. Khalil, CFD history and applications, *CFD Lett.* 4 (2012) 43–46.
- [17] C. Cortés, A. Gil, Modeling the gas and particle flow inside cyclone separators, *Prog. Energy Combust. Sci.* 33 (2007) 409–452, <https://doi.org/10.1016/j.pecs.2007.02.001>.
- [18] F.D.E. Latief, U. Fauzi, S. Bjaksana, Y. Bindar, Pore structure characterization of 3D random pigeon hole rock models, *Int. J. Rock Mech. Min. Sci.* 47 (2010) 523–531.
- [19] N. Sylvia, R. Mutia, Malasari, R. Dewi, Y. Bindar, Yunardi, A computational fluid dynamic comparative study on CO₂ adsorption performance using activated carbon and zeolite in a fixed bed reactor, *IOP Conf. Ser. Mater. Sci. Eng.* 536 (2019) 012042, <https://doi.org/10.1088/1757-899X/536/1/012042>.
- [20] Q. Huang, C. Yang, G. Yu, Z.S. Mao, CFD simulation of hydrodynamics and mass transfer in an internal airlift loop reactor using a steady two-fluid model, *Chem. Eng. Sci.* 65 (2010) 5527–5536, <https://doi.org/10.1016/j.ces.2010.07.021>.
- [21] Z. Li, H. Xu, W. Yang, M. Xu, F. Zhao, Numerical investigation and thermodynamic analysis of syngas production through chemical looping gasification using biomass as fuel, *Fuel* 246 (2019) 466–475, <https://doi.org/10.1016/j.fuel.2019.03.007>.
- [22] Z. Li, H. Xu, W. Yang, A. Zhou, M. Xu, CFD simulation of a fluidized bed reactor for biomass chemical looping gasification with continuous feedstock, *Energy Convers. Manag.* 201 (2019), 112143, <https://doi.org/10.1016/j.enconman.2019.112143>.
- [23] S. Yang, H. Wang, Y. Wei, J. Hu, J.W. Chew, Particle-scale characteristics of the three distinct regions in the multi-chamber slot-rectangular spouted bed, *Powder Technol.* 360 (2020) 658–672, <https://doi.org/10.1016/j.powtec.2019.10.038>.
- [24] S. Nemoda, V. Bakić, S. Oka, G. Živković, N. Crnomarković, Experimental and numerical investigation of gaseous fuel combustion in swirl chamber, *Int. J. Heat Mass Transf.* 48 (2005) 4623–4632, <https://doi.org/10.1016/j.ijheatmasstransfer.2005.04.004>.
- [25] T. Norton, B. Tiwari, D.W. Sun, Computational fluid dynamics in the design and analysis of thermal processes: a review of recent advances, *Crit. Rev. Food Sci. Nutr.* 53 (2013) 251–275.
- [26] S. Steven, E. Restiawaty, P. Pasymi, I.M. Fajri, Y. Bindar, Digitalized turbulent behaviors of air and rice husk flow in a vertical suspension furnace from computational fluid dynamics simulation, *Asia-Pac. J. Chem. Eng.* (2022), <https://doi.org/10.1002/apj.2805>.
- [27] L.E. Ersoy, M. Koksai, F. Hamdullahpur, Effects of mode of secondary air injection on gas and solid velocity profiles in a CFB riser, *Circ. Fluid. Bed Technol. VI* (1999) 417–422.
- [28] C.M.H. Brereton, J.R. Grace, End effects in circulating fluidized bed hydrodynamics, in: *Circ. Fluid. Bed Technol. IV*, 1993, pp. 169–174.
- [29] M. Koksai, Gas Mixing and Flow Dynamics in Circulating Fluidized Beds with Secondary Air Injection, 2001.
- [30] L.V. Ziqiang, L. Guangqiang, L. Yingjie, Optimization study on bias angle of a swirl burner with tangential inlet air, *Int. J. Smart Home* 10 (2016) 171–180, <https://doi.org/10.14257/ijsh.2016.10.3.17>.
- [31] P. Pasymi, Y.W. Budhi, Y. Bindar, Effects of tangential inlet shape and orientation angle on the fluid dynamics characteristics in a biomass burner, *J. Phys. Conf. Ser.* 1090 (2018) 1–8, <https://doi.org/10.1088/1742-6596/1090/1/012007>.
- [32] N. Ngamsidhipongsa, P. Ponpesh, A. Shotipruk, A. Arpornwicheanop, Analysis of the Imbert downdraft gasifier using a species-transport CFD model including tar-cracking reactions, *Energy Convers. Manag.* 213 (2020), 112808, <https://doi.org/10.1016/j.enconman.2020.112808>.
- [33] P. Pasymi, Y.W. Budhi, Y. Bindar, Intrinsic parameters of dry chopped miscanthus for cold particle dynamic modeling, *J. Teknolog.* 82 (2020) 91–100, <https://doi.org/10.11113/jt.v82.13534>.
- [34] S. Steven, P. Hernowo, E. Restiawaty, A. Irawan, C.B. Rasrendra, A. Riza, Y. Bindar, Thermodynamics simulation performance of rice husk combustion with a realistic decomposition approach on the devolatilization stage, *Waste Biomass Valor.* 13 (2022) 2735–2747, <https://doi.org/10.1007/s12649-021-01657-x>.

- [35] T. Defraeye, Advanced computational modelling for drying processes – a review, *Appl. Energy* 131 (2014) 323–344.
- [36] C.G. Speziale, R.M.C. So, Turbulence modeling and simulation, in: *Handbook of Fluid Dynamics*, Second ed., CRC Press, 2016, pp. 1–64.
- [37] ANSYS, ANSYS Fluent Theory Guide 2019 R3, 2019.
- [38] Y. Bindar, *Computational Engineering on Multidimensional Turbulent Flows* (Rekayasa Komputasi Aliran Turbulen Multidimensi), 2017.
- [39] T.R. Vakamalla, K.S. Kumbhar, R. Gujjula, N. Mangadoddy, Computational and experimental study of the effect of inclination on hydrocyclone performance, *Sep. Purif. Technol.* 138 (2004) 104–117.
- [40] A. Haider, O. Levenspiel, Drag coefficient and terminal velocity of spherical and nonspherical particles, *Powder Technol.* 58 (1989) 63–70, [https://doi.org/10.1016/0032-5910\(89\)80008-7](https://doi.org/10.1016/0032-5910(89)80008-7).
- [41] S. Steven, L. Windari, N. Novebriantika, P. Pasymi, E. Restiawaty, Y. Bindar, Investigation of air and rice husk cold flow structures in the suspension furnace chamber through a simulation study, *Int. J. Thermofluid Sci. Technol.* 9 (2022). In press.
- [42] J. Chen, B. Haynes, D. Fletcher, A numerical and experimental study of tangentially injected swirling flow, in: *2nd International Conference on CFD in the Minerals and Process Industries*, 1999, pp. 485–490.
- [43] A. Stroh, F. Alobaid, J.P. Busch, J. Ströhle, B. Eppe, 3-D numerical simulation for co-firing of torrefied biomass in a pulverized-fired 1 MWth combustion chamber, *Energy* 85 (2015) 105–116, <https://doi.org/10.1016/j.energy.2015.03.078>.
- [44] J. Ko, *Numerical Modelling of Highly Swirling Flows in a Cylindrical through-Flow Hydrocyclone*, 2005.
- [45] Y. Bindar, Geometry effect investigation on a conical chamber with porous media boundary condition using computational fluid dynamic (CFD) technique, *J. Eng. Technol. Sci.* 41 (2009) 97–110, <https://doi.org/10.5614/itbj.eng.sci.2009.41.2.1>.
- [46] P. Pasymi, Y.W. Budhi, A. Irawan, Y. Bindar, Three dimensional cyclonic turbulent flow structures at various geometries, inlet-outlet orientations and operating conditions, *J. Mech. Eng. Sci.* 12 (2018) 4300–4328, <https://doi.org/10.15282/jmes.12.4.2018.23.0369>.
- [47] P. Pasymi, Y.W. Budhi, Y. Bindar, The effect of inlet aspect ratio (RIA) to the three dimensional mixing characteristics in tangential burner, *ARNP J. Eng. Appl. Sci.* 12 (2017) 5300–5306.
- [48] S. Purwanto, K. Pudjianto, F. Pradana, Characteristics of powder rice husk burning on cyclone burner, *Int. J. Sci. Technol. Res.* 7 (2018) 127–130.
- [49] J.H. Sosa-amao, D.J.O. Ferreira, C.G. Santos, J.E. Alvarez, L.P. Rangel, S.W. Park, The influence of swirl burner geometry on the sugar-cane bagasse injection and burning, *Int. J. Mech. Mechatron. Eng.* 9 (2015) 864–867.
- [50] M. Rozainee, S.P. Ngo, A.A. Salema, K.G. Tan, Effect of feeding methods on the rice husk ash quality in a fluidised bed combustor, *Emirates J. Eng. Res.* 15 (2010) 1–12.
- [51] C.H. Lin, J.T. Teng, C.S. Chyang, Evaluation of the combustion efficiency and emission of pollutants by coal particles in a vortexing fluidized bed, *Combust. Flame* 110 (1997) 163–172.
- [52] M. Rozainee, *Production of Amorphous Silica from Rice Husk in Fluidised Bed System*, 2007.

5. Penulis Anggota

ORIGINALITY REPORT

18%
SIMILARITY INDEX

15%
INTERNET SOURCES

9%
PUBLICATIONS

5%
STUDENT PAPERS

MATCH ALL SOURCES (ONLY SELECTED SOURCE PRINTED)

< 1%

★ journal.unnes.ac.id
Internet Source

Exclude quotes Off
Exclude bibliography Off

Exclude matches Off